Journal of Alloys and Compounds 509 (2011) 4670–4675

Contents lists available at ScienceDirect

Journal of Alloys and Compounds

journal homepage: www.elsevier.com/locate/jallcom

The stored energy in processed Cu–0.4 wt.%Cr–0.12 wt.%Zr–0.02 wt.%Si–0.05 wt.%Mg

X.F. Li[a], A.P. Dong[b], L.T. Wang[b], Z. Yu[b], L. Meng[a,*]

[a] Department of Materials Science and Engineering, Zhejiang University, Hangzhou 310027, China
[b] China Railway Electrification Bureau Group Co., Ltd., Beijing 100036, China

ARTICLE INFO

Article history:
Received 12 July 2010
Received in revised form 9 January 2011
Accepted 19 January 2011
Available online 26 January 2011

Keywords:
Metals and alloys
Microstructure
X-ray diffraction
Mechanical properties
Thermal analysis

ABSTRACT

Cold drawing was conducted at room temperature to impose high strain on Cu–0.4 wt.%Cr–0.12 wt.%Zr–0.02 wt.%Si–0.05 wt.%Mg. The microstructure was studied by X-ray diffraction and transmission electron microscope. The thermal analysis was carried out for the alloy at different draw ratios and then the stored energy was calculated to estimate the dislocation density and the flow stress. Results indicate that the microstrain gradually increases and the ⟨1 1 1⟩ texture is formed with the draw ratio rising. Meanwhile, the stored energy also increases with the draw ratio rising and a peak is reached with draw ratio of 6.7. The release of stored energy is primarily due to the decrease of dislocation density. The flow stress estimated from the stored energy has a similar variation trend with the measured data with a stress difference ~20 to 120 MPa. The main strengthening effect is attributed to dislocation mechanism.

1. Introduction

Plastic deformation of coarse-grained polycrystalline metals and alloys with a high strain always leads to the refinement of substantial microstructures. And the strain-induced grain refinement process is controlled by the propagation and interaction of dislocations. With the strain increasing, abundant dislocations are generated in coarse grains and form various dislocation structures. These formed dislocation structures gradually transform into sub-boundaries via dislocation interaction subdividing the original coarse grains into refined blocks. Upon further straining, misorientation across the sub-boundaries is enlarged with more dislocation interactions, leading to the forming of grain boundaries. Meanwhile, An obvious strain-hardening and increasing of stored deformation energy can be found.

The stored deformation energy, a portion of the total mechanical energy of deformation, is reserved in the material mostly in the form of dislocation substructures. Therefore, the stored energy is a function of the dislocation density and their spatial structures. The measurements of the stored energy play a crucial role in understanding the dislocation strengthening mechanism of strained metals and alloys. Moreover, understanding the stored energy is very important to control the microstructure evolution and improve the mechanical properties of Cu-based alloys [1–6].

Some studies on the measurements of the stored energy related to the strain degree and recrystallization behavior in polycrystalline metals and alloys with heavy plastic deformation have been presented. Bever et al. [5] and Willams [6] have reported that the ratio of stored energy to plastic work depends on the strain. With strain increasing, the stored energy in high purity copper increased and then reached saturation. The increase of the stored energy produced a concomitant decrease in recrystallization temperature. Once the saturation of the stored energy was attained, the increasing strain did not lead to a further reduction in recrystallization temperature [7,8]. Increasing the grain size decreased the amount of the stored energy at a given strain and increased the recrystallization temperature at low stored energy in pure nickel [9]. The formation and propagation of dislocations during cold deformation led to an increase in stored energy and therefore gave rise to an obvious hardening effect [1,10–13]. The dislocation density was calculated from the total stored energy released in recovery and recrystallization, which corresponded to a reasonable flow stress in cold rolled pure Cu and Fe [1,11]. The saturation of dislocation density, which was not stable enough to form a dislocation boundary inside small grains owing to the strong interactions between dislocations and grain boundaries, may indicate the saturation of stored energy and strain-hardening effect. The saturation of dislocation density is a common phenomenon observed in various metals deformed by severe plastic deformation. Pelton et al. [14], Trybus and Spitzig [15] discovered that the dislocation density of

* Corresponding author. Tel.: +86 57187951027; fax: +86 57187952290.
E-mail address: mengliang@zju.edu.cn (L. Meng).

0925-8388/$ – see front matter.
doi:10.1016/j.jallcom.2011.01.127

the Cu matrix at very high strains does not exceed 10^{11} cm^{-2} as a result of dynamic recovery and recrystallization. Sun [16] also investigated the dynamic recovery and recrystallization of the Cu to minimize the misfit strain between the Cr fibers and the Cu matrix in Cu–15Cr in situ composites.

Cu–Cr–Zr alloys are widely used in engineering applications, such as trolley wires, lead frames, electronic terminals and connectors due to their excellent match between the mechanical strength and the electrical conductivity [17–20]. However, the inherent link between the stored energy and the flow stress in Cu–Cr–Zr alloys, which is connected by the detailed arrangement of dislocations, is still an open question. In this respect, it is important to study the evolution of the microstructure, the characteristics of the dislocation density, the trend of the mechanical property and the stored energy during cold drawing. Cu–0.4 wt.%Cr–0.12 wt.%Zr–0.02 wt.%Si–0.05 wt.%Mg was prepared and then drawn to different draw ratios. The cold drawing behavior was studied by microstructure observation, structure analysis and flow stress measurement. The stored energy was measured and utilized to estimate the dislocation density and flow stress.

2. Materials and experimental methods

Cu–0.4 wt.%Cr–0.12 wt.%Zr–0.02 wt.%Si–0.05 wt.%Mg was melted in a vacuum induction furnace with Ar atmosphere and cast into cylindrical ingots of 20 mm in diameter. Cold drawing deformation was performed at ambient temperature. Drawing ratio was evaluated by $\eta = \ln(A_0/A)$, where A_0 and A were the original and final transverse sectional areas of the drawing specimens, respectively.

The microstructure on longitudinal section of the wire specimens was observed by transmission electron microscope (TEM) on a JEM 2010 instrument operated at 200 kV. TEM foils were sliced from the longitudinal section and prepared by a double jet electropolisher at about −20 °C with an electrolyte of 10% nitric acid and 90% methanol. X-ray diffraction (XRD) analysis was conducted by Cu-K_α radiation ($\lambda = 0.154$ nm). Voigt function based on XRD peak broadening has been employed to calculate the microstrain. Tensile tests were performed on an electronic tensile tester with the strain rate of 2.0×10^{-3} s^{-1}. The flow stress is defined as the stress where the plastic strain is about 0.2%. The thermal analysis was carried out by differential scanning calorimetry (DSC) from 40 to 600 °C with a heating rate of 40 °C/min. The stored energy was taken as the area under the heat releasing peak. For each sample, two DSC runs were obtained and the curve from the second run was used as a baseline. The final DSC curve was the difference between the second run and the first run. Such a procedure is necessary to amplify the extremely small thermal events that occurs in Cu–0.4 wt.%Cr–0.12 wt.%Zr–0.02 wt.%Si–0.05 wt.%Mg.

3. Results and discussion

3.1. Structure evolution

Fig. 1 shows the XRD patterns of the Cu–0.4 wt.%Cr–0.12 wt.%Zr–0.02 wt.%Si–0.05 wt.%Mg at different draw ratios. The XRD patterns not only show the peak distribution of Cu phase but also the relative intensities of peaks changing with the draw ratios. For example, the $(1\,1\,1)_{Cu}$ intensity is the highest in the as-cast specimen but decreases as the draw ratio increases. It is noted that the trend of intensities changes as $6.7 < \eta \leq 7.4$, where the intensity increases dramatically. On the contrary, the $(1\,1\,0)_{Cu}$ intensity is the lowest in the as-cast specimen but increases as the draw ratio rises. These results

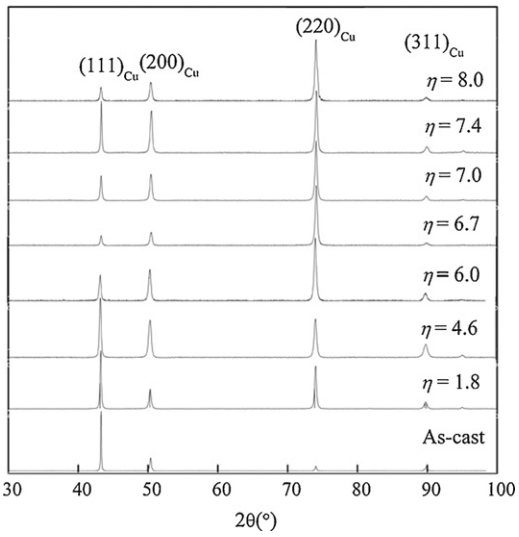

Fig. 1. XRD patterns from longitudinal section of Cu–0.4 wt.%Cr–0.12 wt.%Zr–0.02 wt.%Si–0.05 wt.%Mg at different draw ratios.

indicate that the cold drawing treatment results in the change of crystal orientation in the deformed alloy.

The degree of preferred orientation in the alloy can be calculated by using the Lotgering factor [21]

$$L_{(h\,k\,l)} = \frac{(P_{(h\,k\,l)} - P^0_{(h\,k\,l)})}{(1 - P^0_{(h\,k\,l)})} \quad (1)$$

$$P_{(h\,k\,l)} = \frac{I_{(h\,k\,l)}}{\sum_j I_j} \quad (2)$$

$$P^0_{(h\,k\,l)} = \frac{I^0_{(h\,k\,l)}}{\sum I^0_j} \quad (3)$$

where $I_{(h\,k\,l)}$ and $I^0_{(h\,k\,l)}$ are the intensities of $(h\,k\,l)$ diffraction in the drawn specimens and casting, I_j and I^0_j are the intensities of any diffraction in the drawn specimens and casting, respectively. The difference of crystal orientation between drawn specimen and casting specimen can be reflected by the absolute value of $L_{(h\,k\,l)}$. It is obvious that there is the same crystal orientation between the drawn specimen and the casting specimen if $L_{(h\,k\,l)} = 0$. In general, the greater the absolute value of $L_{(h\,k\,l)}$, the higher the difference of the crystal orientation.

Fig. 2 shows the Lotgering factors of different crystal planes for the alloy on longitudinal sections at different draw ratios, where

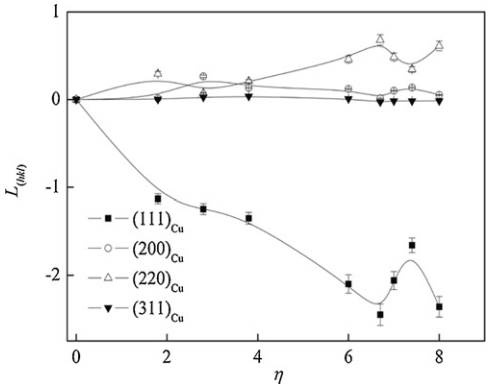

Fig. 2. Lotgering factor dependent on the draw ratio for Cu–0.4%Cr–0.12%Zr–0.02%Si–0.05%Mg.

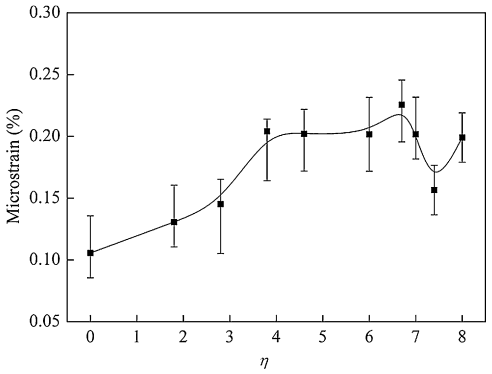

Fig. 3. Microstrain dependent on the draw ratio for Cu–0.4 wt.%Cr–0.12 wt.%Zr–0.02 wt.%Si–0.05 wt.%Mg.

$I^0_{(hkl)}$ and I^0_j are taken from the XRD pattern of the as-cast specimen. The crystal orientation of as-drawn specimen has a relatively big difference with the as-cast specimen. With the draw ratio increasing, the difference increases until it reaches the maximum value when $\eta = 6.7$. However, an opposite trend occurs as $6.7 < \eta \leq 7.4$. These results imply that the drawing deformation results in the change of crystal orientation, but the dynamic recovery occurring in the process of the cold drawing may reduce the preferred orientation.

Fig. 3 shows that the microstrain depends on the draw ratio. The XRD pattern of the annealed Cu was used as the standard pattern without microstrain for the calculation of the microstrain. It is clear that cold drawing induces a gradual increase in microstrain and the peak value reaches at $\eta = 6.7$. At higher draw ratios, there is a slight decrease in microstrain, the reason of which is that the stored energy was released to a certain degree and the internal stress was partially relaxed by recovery. Previous investigations showed that microstrain in high purity Cu samples processed by different approaches varied in a wide range, such as 0.1% in equal-channel angular pressing Cu [22], 0.2% in ball-milled Cu [23], 0.24% in magnetron sputtering Cu [24] and 0.16% in conventional cold rolling Cu [1]. The present results are consistent with those in the cold worked Cu samples reported in the literature [1,22–24].

3.2. Microstructure

Fig. 4(a) and (b) shows a bright field TEM micrograph and the corresponding selected area electron diffraction pattern (SADP) of the Cu–0.4 wt.%Cr–0.12 wt.%Zr–0.02 wt.%Si–0.05 wt.%Mg on longitudinal direction at $\eta = 6.7$. The typical filamentary structure aligns uniformly along the wire axis with a mean width of ~490 nm. It is noticed that the diffraction spots from the Cu matrix in the ⟨1 1 1⟩ direction are slightly elongated, as indicated by the arrows in Fig. 4b. It implies that Cu filaments have a preferred orientation with small angle boundaries in the ⟨1 1 1⟩ direction. Fig. 4(c) and (d) show the SADP of A and B fibers in Fig. 4(a), respectively. Weak diffraction spots are observed in Fig. 4(d) as indicated by arrows. These weak diffraction spots should come from fine precipitates. Fig. 4(e) shows the magnified TEM image of B area and

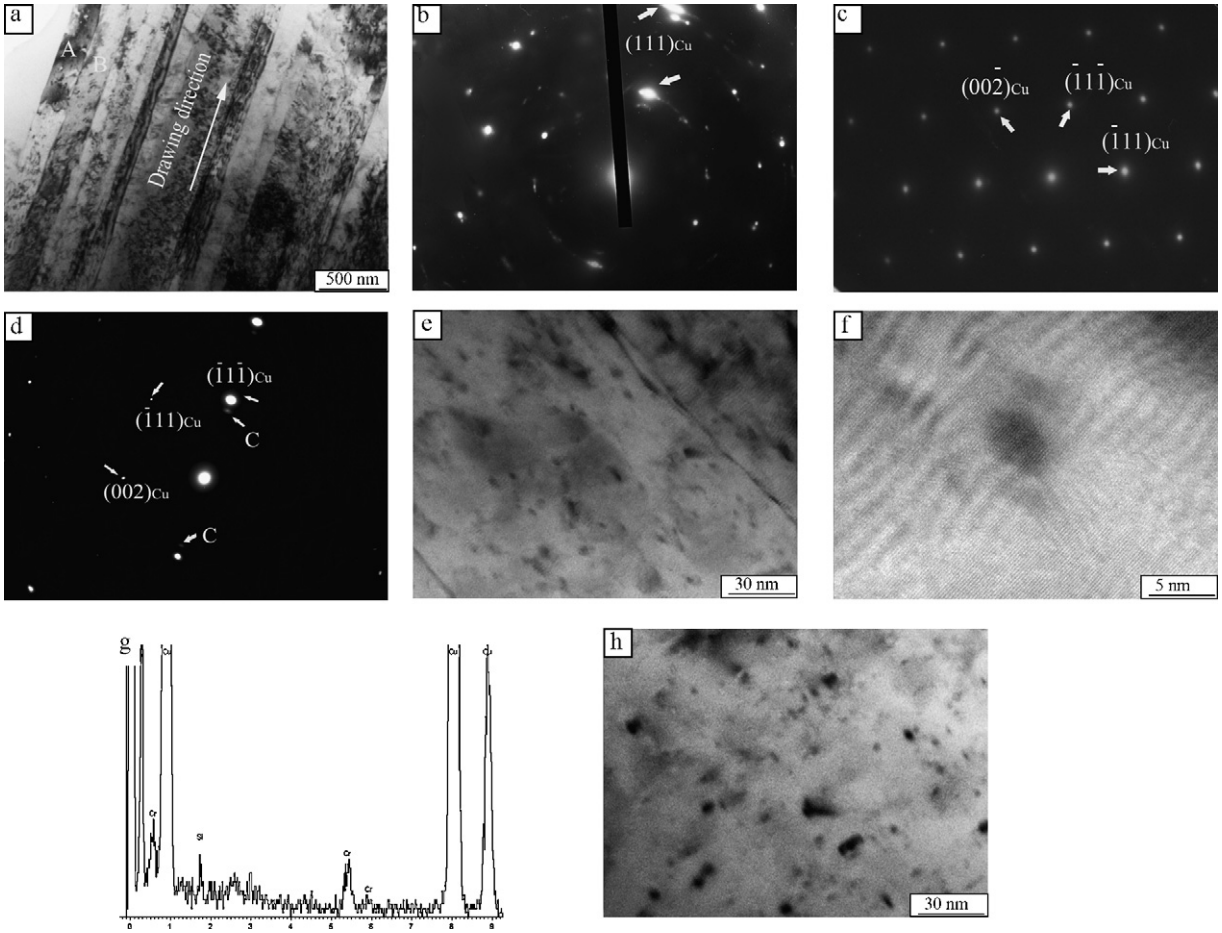

Fig. 4. (a) TEM images on longitudinal section of Cu–0.4 wt.%Cr–0.12 wt.%Zr–0.02 wt.%Si–0.05 wt.%Mg with $\eta = 6.7$; (b) corresponding SADP pattern of total area; (c) A area; (d) B area; (e) distribution of the precipitates of area B; (f) a detailed observation of the precipitates; (g) the EDX of the precipitates; (h) distribution of the precipitates annealed at 300 °C for 1 h.

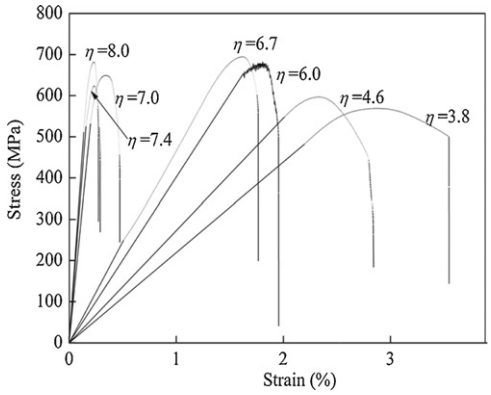

Fig. 5. Tensile stress–strain curves of the Cu–0.4 wt.%Cr–0.12 wt.%Zr–0.02 wt.%Si–0.05 wt.%Mg with various drawing ratios.

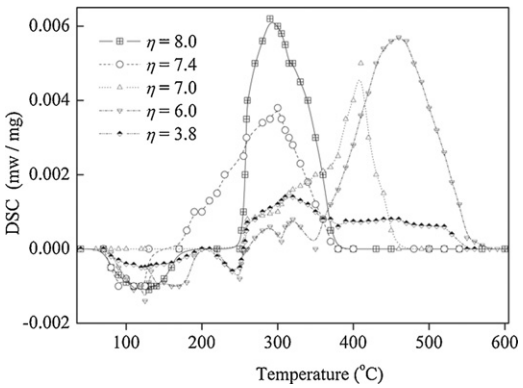

Fig. 6. Heat flow difference of two consecutive runs at 40 °C/min for Cu–0.4 wt.%Cr–0.12 wt.%Zr–0.02 wt.%Si–0.05 wt.%Mg (η = 3.8, 6.0, 7.0, 7.4, 8.0).

fine precipitates are clearly observed inside the Cu matrix. Most of the precipitates exhibit spherical or nearly spherical shape with a size in the range 3–7 nm in diameter (Fig. 4(f)). The energy dispersive X-ray (EDX) test shows these precipitates are rich in Cr and Si elements, suggesting the precipitates are CrSi compounds (Fig. 4(g)). Fig. 4(h) shows a TEM micrograph of the alloy annealed at 300 °C for 1 h. The size of the precipitates becomes slightly larger than that under drawn condition, ranging 5–15 nm in diameter. This indicates that the precipitate growth takes place during heat treatment.

3.3. Strength

Fig. 5 shows the tensile stress–strain curves of Cu–0.4 wt.%Cr–0.12 wt.%Zr–0.02 wt.%Si–0.05 wt.%Mg at different drawing ratios. Tensile tests of various samples at ambient temperatures indicate that Cu–0.4 wt.%Cr–0.12 wt.%Zr–0.02 wt.%Si–0.05 wt.%Mg exhibits a flow stress of ~670 MPa and an ultimate tensile strength of ~700 MPa with η = 6.7. With extending plastic deformation, there is a slight decrease in the flow stress with $6.7 < \eta \leq 7.4$. Cold drawing induces an obvious increase in strength but a decrease in tensile elongation. With η = 3.8, the flow stress and the ultimate tensile strength decrease to ~550 MPa and ~570 MPa, respectively. Table 1 shows the flow stress and the ultimate tensile strength of Cu–0.4 wt.%Cr–0.12 wt.%Zr–0.02 wt.%Si–0.05 wt.%Mg at different draw ratios.

3.4. DSC

Fig. 6 shows the heat flow of the calorimeter in an experiment starting at 40 °C. The DSC curve shows exothermic reaction points in the positive *y*-direction. The DSC curve, including initial endothermal peaks and subsequent exothermal peak, reveals the complexity of multistage structural transformations in Cu–0.4 wt.%Cr–0.12 wt.%Zr–0.02 wt.%Si–0.05 wt.%Mg under linear heating. The initial endothermal peaks can be attributed to the dissolution of the solute clusters formed in dislocation walls at low temperatures [10]. The subsequent exothermal peak can be associated with the annihilation of some defects and the precipitation of some secondary particles during recovery. As mentioned in Fig. 4, the precipitates are CrSi compounds and the precipitates growth takes place after annealing at 300 °C for 1 h. Previous investigations have showed precipitation kinetics in binary Cu–Cr, Cu–Zr and ternary Cu–Cr–Zr alloy [25,26]. The first exothermal reaction is noticed at about 220 °C and the order of precipitation is Cu_3Zr and Cr appearing at about 350 °C and 425 °C in cold-worked specimen, respectively [25]. The order of precipitation and the corresponding temperature of exothermal peak depend on pre-strain history. It has long been understood that the strain degree of cold working will accelerate the rate of precipitation [26]. Only one large exothermal peak is observed at high temperatures, which corresponds to the sufficient release of the stored energy during recrystallization when dislocation density significantly decreases.

The values of the stored energy released in the recrystallization process could be obtained by calculating the area under the large exothermal peak [1,2,27]. Table 2 shows the values of the stored energy calculated from the exothermal peak at different draw ratios. The released stored energy is different, ranging from 30.1 J/mol (η = 3.8) to 128.1 J/mol (η = 6.7).

In ultrafine-grained metals, the majority of stored energy released during recrystallization is attributed to the disappearance of high-density grain boundaries and dislocations. The contributions from other defects such as vacancies and the associated elastic strain energy are minor [11,28,29]. The possible contribution from grain boundaries to the recrystallization exotherm can be estimated as follows: The total surface energy per unit volume attributing to grain boundaries E_{gb} is given as $2\nu/D$, where ν is grain boundary energy per unit area and D the filament size. Taking ν as 0.6 J/m^2 for Cu [28–30] and D as ~550 nm (η = 6.0), the grain boundary energy contributing to the stored energy is $\sim 2.2 \times 10^6$ J/m^3 or 15.7 J/mol. At low strain, the grain boundary surface energy is so low that it is neglected in this analysis. For example, D is ~240 μm with η = 1.8 and the grain boundary energy contributing to the stored energy is ~0.036 J/mol. The grain boundary energy and the average filament size at different ratios are listed in Table 2.

In a heavily drawn alloy, strength can be well correlated to the dislocation density using Taylor approach which strengthening is mainly caused by dislocation–dislocation interactions [10,11,28]. The flow stress σ related to the dislocation density can be expressed as

$$\sigma = \sigma_o + \alpha M G b \rho^{1/2} \quad (4)$$

where σ_o is the friction stress, M the Taylor factor (M = 3 for polycrystalline materials [28]), α a dimensionless number ($\alpha \approx 1/3$ is taken [1]), G the shear modulus (G = 47 GPa for Cu [28]) and b the Burgers vector (b = 0.256 nm in Cu lattice [28]). The dislocation density can be related to the stored energy in terms of $\rho = (E_s - E_{gb})/E_d$, where E_d is the energy per unit length of a dislocation and an average value of 5×10^{-9} J/m is taken without making any distinction between edge or screw dislocations, complete or partial dislocations [11,29].

The microstrain can be related to the dislocation density by $\rho = 16.1 \times \varepsilon^2/b^2$ [27], where ε is the microstrain and b is the Burgers vector (b = 0.256 nm in Cu lattice [28]). The dislocation densities of various samples derived from the microstrain and the stored energy

Table 1
The flow stress and ultimate tensile strength of Cu–0.4 wt.%Cr–0.12 wt.%Zr–0.02 wt.%Si–0.05 wt.%Mg at different draw ratios.

η	3.8	4.6	6.0	6.7	7.0	7.4	8.0
Flow stress (MPa)	550 ± 10	575 ± 10	660 ± 20	670 ± 15	620 ± 15	600 ± 15	650 ± 15
Ultimate tensile strength (MPa)	557 ± 10	600 ± 15	665 ± 20	700 ± 25	650 ± 15	615 ± 15	680 ± 20

Table 2
The DSC measurement results on E_s and calculated E_{gb}.

Draw ratio (η)	3.8	6.0	6.7	7.0	7.4	8.0
E_s (J/mol)	30.1 ± 1.20	90.6 ± 1.10	128.1 ± 0.80	65.1 ± 1.20	46.8 ± 1.30	74.2 ± 0.80
Average filament size (nm)	1020 ± 20	550 ± 10	490 ± 8	610 ± 16	620 ± 15	540 ± 12
E_{gb} (J/mol)	8.43 ± 0.08	15.7 ± 0.06	17.6 ± 0.05	14.1 ± 0.06	13.9 ± 0.06	15.9 ± 0.08

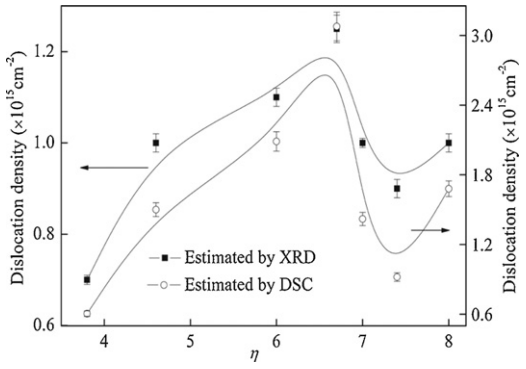

Fig. 7. Dislocation density of Cu–0.4 wt.%Cr–0.12 wt.%Zr–0.02 wt.%Si–0.05 wt.%Mg estimated by XRD and DSC, respectively.

measurements are showed in Fig. 7. A similar variation trend has been observed. The value estimated by DSC is higher than that by XRD. A previous study indicated that the samples have a little higher dislocation density ($1.0 \times 10^{15}\ m^{-2}$) than the reported results from other groups derived from XRD measurements of nano-grained Cu ($0.7 \times 10^{15}\ m^{-2}$) after cold drawing [1].

If it is supposed that the dislocation density can be ignored in the alloy after full annealing, we can take the flow stress 190 MPa of the specimens annealed at 700 °C as the value of the friction stress σ_o in the investigation. Fig. 8 shows σ_e and σ_t dependent on the draw ratios for Cu–0.4 wt.%Cr–0.12 wt.%Zr–0.02 wt.%Si–0.05 wt.%Mg, where σ_e is the flow stress obtained by Eq. (4) and σ_t is the flow stress measured by tensile test.

It is reasonable that the estimated flow stress will be high because the friction stress measured contains alloying strengthening causing by precipitation in particular CrSi compounds

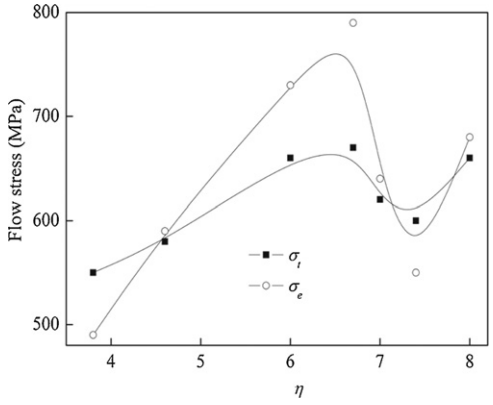

Fig. 8. The estimated flow stress σ_e and the measured flow stress σ_t dependent on draw ratios for Cu–0.4 wt.%Cr–0.12 wt.%Zr–0.02 wt.%Si–0.05 wt.%Mg.

[17,25–33]. In general, there is a similar variation trend between the estimated values and the measured data with a stress difference of 20–120 MPa. This difference may be attributed to the high-energy boundaries existing in high strain [27]. It indicates the dislocation interactions play a dominant role in strengthening effect for Cu–0.4 wt.%Cr–0.12 wt.%Zr–0.02 wt.%Si–0.05 wt.%Mg.

4. Conclusions

With the strain increasing, the crystal orientation in processed Cu–0.4 wt.%Cr–0.12 wt.%Zr–0.02 wt.%Si–0.05 wt.%Mg is deviating from the as-cast specimens and the ⟨1 1 1⟩ texture is formed. The dislocation density of the alloy is gradually increasing with the draw ratio rising before $\eta \leq 6.7$, resulting in the increase of microstrain, strength, and stored energy.

The dynamic recovery has taken place as $6.7 < \eta \leq 7.4$, which is confirmed by the change of the crystal orientation, microstrain, stored energy, flow stress and dislocation density.

The release of stored energy is primarily due to the decrease of dislocation density. There is a similar variation trend of the flow stress between the estimated values from the stored energy and the measured data with a stress difference ~20 to 120 MPa in processed Cu–0.4 wt.%Cr–0.12 wt.%Zr–0.02 wt.%Si–0.05 wt.%Mg. The main strengthening effect of Cu–0.4 wt.%Cr–0.12 wt.%Zr–0.02 wt.%Si–0.05 wt.%Mg is attributed to dislocation mechanism.

Acknowledgment

The project is supported by the National Science and Technology Pillar Program of China (Grant No. 2009BAG12A09).

References

[1] Y. Zhang, N.R. Tao, K. Lu, Acta Mater. 56 (2008) 2429–2440.
[2] J.E. Bailey, P.B. Hirsch, Proc. Roy. Soc. A. 267 (1962) 11.
[3] M.F. Ashby, Philos. Mag. 21 (1970) 399–424.
[4] S.H. Choi, Acta Mater. 51 (2003) 1775–1788.
[5] M.B. Bever, D.L. Holt, A.L. Titchene, Prog. Mater. Sci. 17 (1972) 5–177.
[6] R.O. Williams, Acta Mater. 9 (1961) 949–957.
[7] L. Liu, I. Baker, Scripta Mater. 28 (1993) 197–200.
[8] Y. Zhang, J.T. Wang, C. Cheng, J.Q. Liu, J. Mater. Sci. 43 (2008) 7326–7330.
[9] I. Baker, L. Liu, D. Mandal, Scripta Mater. 32 (1995) 167–171.
[10] M. Verdier, I. Groma, L. Flandin, J. Lendvai, Y. Brechet, P. Guyot, Scripta Mater. 37 (1997) 449–454.
[11] F. Scholz, J.H. Driver, E. Woldt, Scripta Mater. 40 (1999) 949–954.
[12] D. Mandal, I. Baker, Scripta Mater. 33 (1995) 831–836.
[13] A. Godfrey, W.Q. Cao, N. Hansen, Q. Liu, Metall. Mater. Trans. A. 36A (2005) 2371–2378.
[14] A.R. Pelton, F.C. Laabs, W.A. Spitzig, C.C. Cheng:, Ultramicroscopy 22 (1987) 251–265.
[15] C.L. Trybus, W.A. Spitzig, Acta Mater. 37 (1989) 1971–1981.
[16] S.J. Sun, Metall. Mater. Trans. A 32 (2001) 1225–1232.
[17] D.L. Zhang, K. Mihara, S. Tsubokawa, H.G. Suzuki, Mater. Sci. Technol. 16 (2000) 357–363.
[18] W.X. Qi, J.P. Tu, F. Liu, Y.Z. Yang, N.Y. Wang, H.M. Lu, X.B. Zhang, S.Y. Guo, M.S. Liu, Mater. Sci. Eng. A 343 (2003) 89–96.

[19] S.G. Mu, F.A. Guo, Y.Q. Tang, X.M. Cao, M.T. Tang, Mater. Sci. Eng. A 475 (2008) 235–240.
[20] P. Marmy, J. Nucl. Mater. 329A (2004) 188–192.
[21] F.K. Lotgering, J. Inorg. Nucl. Chem. 9 (1959) 113.
[22] F. Dalla Torre, R. Lapovok, J. Sandlin, P.F. Thomson, C.H.J. Davies, E.V. Pereloma, Acta Mater. 52 (2004) 4819–4832.
[23] J.Y. Huang, Y.K. Wu, H.Q. Ye, Acta Mater. 44 (1996) 1211–1221.
[24] L.H. Qian, S.C. Wang, Y.H. Zhao, K. Lu, Acta Mater. 50 (2002) 3425–3434.
[25] A. Vinogradov, V. Patlan, Y. Suzuki, K. Kitagawa, V.I. Kopylov, Acta Mater. 50 (2002) 1639–1651.
[26] G.C. Smith, Prog. Metal Phys. 2 (1949) 163–243.
[27] G.K. Willimson, R.E. Smallman, Philos. Mag. 1 (1956) 34–46.
[28] J. Gubicza, N.Q. Chinh, G. Krallics, I. Schiller, T. Ungar, Curr. Appl. Phys. 6 (2006) 194–199.
[29] A. Rohatgi, K.S. Vecchio, Mater. Sci. Eng. A 328 (2002) 256–266.
[30] A. Rohatgi, K.S. Vecchio, G.T. Gray, Acta Mater. 49 (2001) 427–438.
[31] L.E. Murr, Interfacial Phenomena in Metals and Alloys, Addison-Wesley, Reading, MA, 1975.
[32] P. Liu, B.X. Kang, X.G. Cao, J.L. Huang, B. Yen, H.C. Gu, Mater. Sci. Eng. A 265 (1999) 262–267.
[33] J.H. Su, Q.M. Dong, P. Liu, H.J. Li, B.X. Kang, Mater. Sci. Eng. A 392 (2005) 422–426.